Surfaces and Interfaces 28 (2022) 101660

Contents lists available at ScienceDirect

Surfaces and Interfaces

journal homepage: www.sciencedirect.com/journal/surfaces-and-interfaces

In-situ grown nanoscale p-n heterojuction of Cu_2S-TiO_2 thin film for efficient photoelectrocatalytic H_2 evolution

Satya Veer Singh [a], Urwashi Gupta [b], Sajal Biring [*,c], Bratindranath Mukherjee [*,b], Bhola N. Pal [*,a,c]

[a] School of Materials Science and Technology, Indian Institute of Technology (Banaras Hindu University), Varanasi, 221005, India
[b] Department of Metallurgical Engineering, Indian Institute of Technology (Banaras Hindu University), Varanasi, 221005, India
[c] Organic Electronics Research Center and Department of Electronic Engineering, Ming Chi University of Technology, New Taipei City, Taiwan 243, Taiwan, ROC

ARTICLE INFO

Keywords:
Sol-gel
Cu_2S NPs
Titanium dioxide
Photoelectrocatalysis
H_2 generation

ABSTRACT

Nanoscale heterojuction thin film of Cu_2S-TiO_2 has been grown by sol-gel technique and has been employed for efficient H_2 production through water splitting. This nanoscale heterojunction has been grown in three steps which include ion conducting $Li_4Ti_5O_{12}$ thin film deposition and ion-exchange ($Li^+ \leftrightarrow Cu^+$) followed by a sulfurization process. To study the photoelectrochemical performance of this Cu_2S-TiO_2 heterojunction thin film, photoanodes were fabricated on TiO_2 coated FTO substrate. The TiO_2 film was deposited by two different methods - the sol-gel method and colloidal TiO_2 nanoparticles (TiO_2—NP). Highest photocurrent of ~36 $mAcm^{-2}$ was obtained by Cu_2S-TiO_2/TiO_2—NP/FTO photoanode under 0.5 V potential (E Vs. RHE, 1 M KOH). The photocurrent is $\sim 10^3$ times higher compared to that of the bare TiO_2 photoanode and stable for several hours. The photoelectrochemical (PEC) behavior is much higher with respect to previous reports on Cu_2S (NP)-TiO_2 nanocomposite photoanodes, which is due to the significant reduction in carrier recombination at the electronically coupled Cu_2S-TiO_2 heterojunction interface.

1 Introduction

Efficient hydrogen generation by using solar light via water splitting is a demanding area of research for a clean and sustainable energy conversion process [1]. Traditionally, titanium dioxide (TiO_2) is used for photocatalytic H_2 generation applications because of its high environmental stability, lower cost and its capability to purify water by destruction of organic compounds. [1,2], However, the efficiency of this wide gap (E_g~3.2 eV) TiO_2 is critically limited for the utilization of visible light [3,4]. Therefore, till date, several methods have been used to improve its absorption, including metal, nonmetal, and metallic ion doping that are capable of reducing its bandgap and enhancing the photocatalytic properties under visible light [5–7]. In addition, the deposition of atmospherically stable metal nanoparticles (Ag, Au, Al, Pd) [8,9–11] in combination with TiO_2 can improve the photo-electrocatalytic efficiency via hot-electron generation by surface plasmon resonance that effectively enhanced photocurrent generation [12, 13] . Besides, an alternative way to enhance the absorption of TiO_2 is by heterojunction formation with lower bandgap metal sulfides (M_2S such as M = Ag, Cu) [14,15]. However, to date, photo-electrocatalytic efficiency of M_2S-TiO_2 heterojunction photoanode is not very efficient, because of its low charge separation rate through the interface of heterojunction. [16,17] Therefore, it is required to develop a technique for the creation of superior electrical contact of M_2S and TiO_2 to control the band offset, which is the driving force at the interface of these two semiconductors for the interfacial charge transfer process [18,19].

So far, a series of M_2S-TiO_2 heterojunctions, including CdS [20–23], Cu_2S [14], Ag_2S [15] MoS_2 [24] NPs, have been widely studied, which are commonly deposited on top of the TiO_2 surfaces. Among them, Cu_2S is considered an excellent candidate because of its ideal bandgap (1.2 eV) [25, 26] high absorption coefficient ($>10^4$ cm^{-1}), and good semiconducting nature [18,25]. Instead of that, the performance of Cu_2S NP for photoelectrochemical based H_2 generation is still very low, which is due to the poor heterojunction formation between Cu_2S and TiO_2 with considerably high interface trap state [27,28,18]. Therefore, in this study, electronically coupled Cu_2S NP has been grown inside TiO_2 thin films and have used for photoelectrocatalytic H_2 production. In this growth process, uniform and wide-area Cu_2S-TiO_2 thin films are

* Corresponding authors.
E-mail addresses: biring@mail.mcut.edu.tw (S. Biring), bratindra.met@iitbhu.ac.in (B. Mukherjee), bnpal.mst@iitbhu.ac.in (B.N. Pal).

https://doi.org/10.1016/j.surfin.2021.101660
Received 29 August 2021; Received in revised form 25 November 2021; Accepted 4 December 2021
Available online 7 December 2021

fabricated that contain Cu_2S NP with diameters ranging from 10 to 20 nm. The photo-electrocatalytic properties of Cu_2S-TiO_2 nano-heterojunction were studied by photo-electrochemical water splitting experiments as discussed in the following sections.

2. Experiment

2.1. Material synthesis and electrode fabrication

In this work all Cu_2S(NP)-TiO_2 thin films were fabricated by using Fluorine-doped Tin Oxide (FTO) glass substrate. To improve the photoelectrochemical performance of the photoanode, a layer of TiO_2 was grown on top of FTO glass prior to the growth of Cu_2S(NPs)-TiO_2 films. Two different types of TiO_2 layers were used in our experiment. One of them has been deposited by sol gel technique (TiO_2 (sol gel)) and the other one has been deposited from commercial TiO_2 nanoparticle (TiO_2–NP) purchased from Greatcell Solar materials (18NR-T). The sol gel film of TiO_2 was grown from 300 mM precursor solution of titanium (IV) butoxide [$Ti(OC_4H_9)_4$] solution, whereas TiO_2 NP film was deposited from a colloidal solution of TiO_2 NP (20 mg/ml) through a spin coating method (5000 rpm) and successive annealing process (500 °C, for 30 min). Overall three different types of photoanodes were fabricated which are Cu_2S(NP)-TiO_2/FTO, Cu_2S(NP)-TiO_2 /TiO_2 (sol gel)/FTO and Cu_2S(NP)-TiO_2 /TiO_2 NP/FTO. Besides, a reference photoanode was fabricated without Cu_2S(NP)-TiO_2 layer (TiO_2 (sol gel)/FTO. Subsequently, Cu_2S-TiO_2 nanoheterojunction thin film was deposited by chemical route. For this, a $Li_4Ti_5O_{12}$ thin film was deposited on top of the FTO or TiO_2 coated FTO substrate by sol gel method. To grow this ion conducting ceramic film, 300 mM of titanium butoxide [$Ti(OC_4H_9)_4$] was mixed with 300 mM lithium acetate (4:5 by volume). Citric acid solution was added (with a metal to acid ratio~0.5) with this mixture to stabilize the sol and was stirred at room temperature under air ambient conditions that resulted a clear sol after 5 h of stirring. This precursor sol was used for growing $Li_4Ti_5O_{12}$ thin film through dip coating method on various substrates (FTO, TiO_2 (sol gel)/FTO, and TiO_2 NP/FTO of size 20 × 30 mm^2) with a dipping/drawing rate of 2 $mm.sec^{-1}$. Afterwards, all these substrates have been annealed at 550 °C in air for 60 min to obtain a crystalline phase of $Li_4Ti_5O_{12}$ thin film [29,30]. This $Li_4Ti_5O_{12}$ deposition procedure has been repeated two times more to get the desired film thickness of $Li_4Ti_5O_{12}$ (~60 nm). Then the entire substrate was immersed into a copper (I) chloride solution (inside 100 mM) at room temperature for 60 min that allows copper ion (Cu^+) of solution to exchanges with lithium ion (Li^+) of the $Li_4Ti_5O_{12}$ to form $Cu_4Ti_5O_{12}$ thin film through an ion-exchange process. Afterwards, substrates were dipped in a distilled (DI) water for removing unreacted Cu(I)Cl from the surface. Following to this process, clean $Cu_4Ti_5O_{12}$ thin films were immersed into a Na_2S solution (300 mM) that convert Cu^+ to Cu_2S to form Cu_2S-NC, and the original $Cu_4Ti_5O_{12}$ crystal changes to TiO_2 to grow Cu_2S (NP)-TiO_2 nanoheterojunction thin film. After growth, all these substrates were cleaned in DI water to wash out unreacted Na_2S from the surface of the film. This entire chemical growth process is shown schematically in Fig. 1. Related chemical reactions of this growth process is shown in equation 1(a-c).

$$Li_4Ti_5O_{12} + 4Cu(I)Cl + H_2O \rightarrow Cu_4Ti_5O_{12} + 4LiCl + H_2O \quad (a)$$

$$Cu_4Ti_5O_{12} + 3Na_2S + 4H_2O \rightarrow \mathbf{2Cu_2S + 5TiO_2} + 6NaOH + H_2S \quad (b)$$

$$Cu_4Ti_5O_{12} + 6Na_2S + 6H_2O \rightarrow \mathbf{2Cu_2S + 5TiO_2} + 8NaOH + 4NaSH \quad (c)$$

2.2. Materials characterization

The crystal phases of different thin films were identified by X-ray diffraction method (Rigaku XRD with Cu-Kα (λ = 1.54 Å) radiation. The surface morphology and the microstructure of different thin films were studied by high-resolution scanning electron microscopy (HR-SEM, Nova Nano SEM 450). Different nanostructure and nanoheterojunction formation were studied with a transmission electron microscopy (TEM, Tecnai G2 20 TWIN). The TEM sample of Cu_2S (NP)-TiO_2 was prepared by scratching the thin film of Cu_2S (NP)-TiO_2 from the substrate followed by a grinding process by a mortar pestle. Afterwards, colloidal solution of this powder was prepared by using chloroform as solvent. Solution was kept in an ultrasonic bath for 60 min to dispersed the particles which were taken on a carbon coated grid for TEM study. The elemental binding energies of Cu_2S (NP)-TiO_2 sample was studied by X-ray photoelectron spectroscopy (XPS) method (Thermo Fisher Scientific, Al-K_α 1063). The UV–visible absorption properties of different thin films were studied by using a UV–vis spectrophotometer (Shimadzu UV-3600).

2.3. Electrochemical measurements

Photoelectrochemical (PEC) properties of different photoanodes were studied by using photoanode as a working electrode with a three electrode system. A schematic figure of this experimental set-up is given in the supporting document (Fig. S1). A platinum (Pt) plate and a

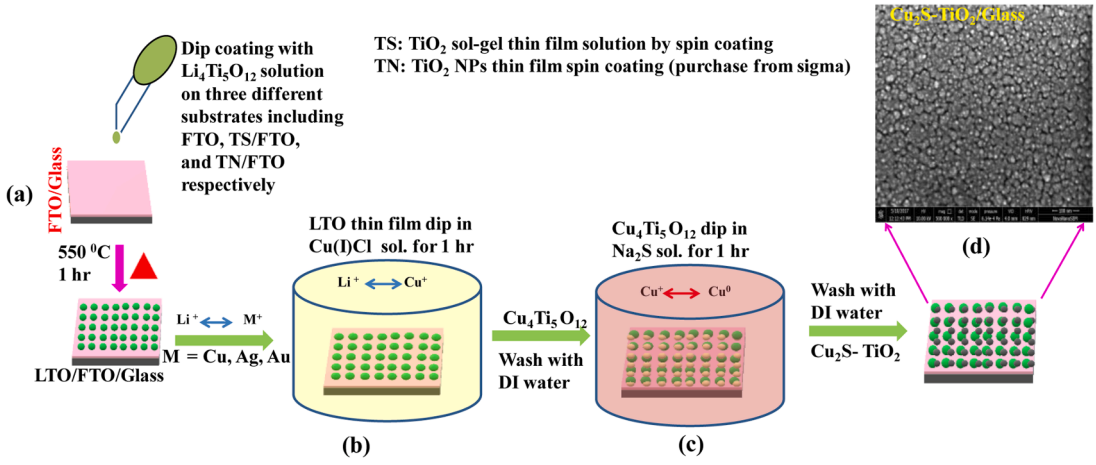

Fig. 1. The schematic presentation of growth steps of Cu_2S (NPs)-TiO_2 thin film a) $Li_4Ti_5O_{12}$ precursor film coated on substrate by dip coating method and subsequent annealing of the precursor film at 550 °C for 60 min b) dipping the sample inside Cu(I)Cl to replace Li^+ of the film by Cu^+ by ion-exchange method, c) Sulfurization processes that convert $Cu_4Ti_5O_{12}$ to Cu_2S-TiO_2 heterojunction film, d) Scanning electron micrograph (SEM) of the upper surface of Cu_2S-TiO_2 heterojunction films.

saturated Ag/AgCl (in 1 M KOH solution) were chosen as the counter electrode and reference electrode respectively. For white light illumination, a xenon light source has been used with an intensity of 100 mW/cm^2. Photocurrents were measured by using a Corr Test/Electrochemical and Corrosion Studio 5 [Model CS350 I COM4 SN: CS3501609178]. The same potentiostat has been used to measure electrochemical impedance spectra (EIS). All measured potential has been referenced to a reversible hydrogen electrode (RHE) by the measured applied potential (versus Ag/AgCl), which was converted into a reversible hydrogen electrode (RHE) by using the Nernst equation [31]. The efficiency of photoanodes were calculated by measuring Incident photon-to-current efficiency (IPCE) by using the following equation [32].

$$\text{IPCE}=\frac{\text{effective photons or generated charges at the interface}}{\text{incident photon}}=\frac{1240\times J_{ph}}{P\times\lambda}\times 100\%$$

Where J_{ph} is the photocurrent density (in mAcm^{-2}), P is the input power of illuminated light (in Wcm^{-2}) and λ is the wavelength of light (in nm).

Photoelectrocatalytic H_2 Evolution Test: The H_2 evolution experiments were performed within a 100 mL Teflon beaker reactor (shown in the fig. S2) at ambient conditions with a sealed silicone rubber pipe and Teflon tape. A 100 W xenon arc-lamp has been used as a white-light source to start the PEC reaction with a focused intensity of 100 mW/cm^2 which was illuminated on photoanodes of size 20 × 30 cm^2. The spectrum of xenon arc-lamp has been shown in supporting document (Fig. S8). The 1 MKOH solution was used as an electrolyte, and potential was varied from –0.5 to 0.4 V. Before starting the experiment, argon gas was passed through the set-up for 10 min to remove the air, so that all the reaction can be performed in an inert atmospheric condition.

2.4. Impedance spectroscopy study

The internal impedance was determined after HER measurement by electrochemical impedance spectroscopy (EIS) study by varying frequency from 1 MHz to 0.1 Hz under an open-circuit voltage (OCV) of 0.5 V, which is capable to determine internal resistance free (iR-free) potential of the working-electrode.

3. Results and discussions

3.1. Structural and surface morphology characterization

The x-ray diffraction (XRD) pattern of pure TiO_2 and $Li_4Ti_5O_{12}$ (LTO) thin film has been shown in Fig. 2(a). The XRD pattern of $Li_4Ti_5O_{12}$ indicates diffraction peaks at 2θ ~ 18.5°, 35.6°, 43.7°, that refers to diffraction planes of (111), (311), (331), respectively. Those peak positions are well-matched with JCPDS file no. 490207, indicating its cubic-spinel crystal structure with the space group of (F $\bar{3}$dm). The XRD peaks of TiO_2 are identified at 2θ ~25.36°, 37.88°, 48.11°, 54.12° which are due to the diffraction plane of (101), (004), (200), (105), respectively (JCPDS No. 894921), implying its tetragonal structure with the space group of ($I4_1$). This figure also shows diffraction peaks of Cu_2S-TiO_2 thin film with the peak positions at 2θ ~33.45°, 45.96°, that corresponds to diffraction planes of (102) and (110) of Cu_2S (JCPDS file number 892,670). Besides, XRD pattern of Cu_2S-TiO_2 sample reveals the formation of the anatase phase of TiO_2 that has a peak position at 2θ ~25.45° and 54.25°. [5,33]

The UV–VIS absorption spectra of different Cu_2S-TiO_2 thin films on various substrates and pure TiO_2 thin films are shown in Fig. 2(b) within the spectral range of 300–900 nm. As expected, the absorption spectra of TiO_2 shows a very strong absorption in the UV region (300 nm) due to its wide bandgap TiO_2 (3.3 eV). However, all those Cu_2S-TiO_2 thin films show significantly higher absorption due to the much lower bandgap of Cu_2S (1.2 eV) [26] nanocrystal that grows inside TiO_2. The bandgap of both TiO_2 and Cu_2S-TiO_2 thin films were calculated by Tauc plot which are 3.3 and 1.6 eV (fig. S3), which are quite similar to the previous

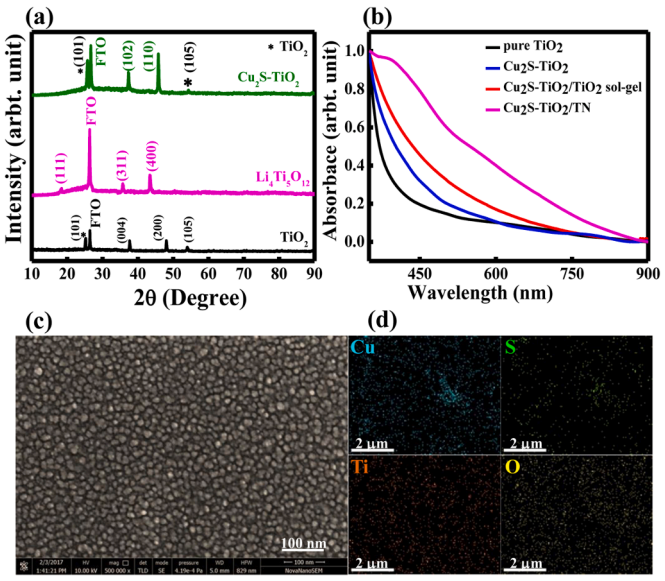

Fig. 2. (a) The x-ray diffraction pattern of pure TiO_2, $Li_4Ti_5O_{12}$ and Cu_2S-TiO_2 thin film (b) Normalized UV–VIS absorption spectra of pure TiO_2 and Cu_2S-TiO_2 thin films coated on three different substrates (on FTO, TiO_2 (sol-gel)/FTO, and TiO_2 NP//FTO) (c) The scanning electron microscope (SEM) image of Cu_2S-TiO_2 thin film (d) Elemental mapping of Cu_2S-TiO_2 thin film.

reported works on Cu_2S-TiO_2. [34,35]

The surface morphology and structural analysis of Cu_2S-TiO_2 thin film were studied by scanning electron microscopy (SEM), as shown in Fig. 2(c). All these Cu_2S-TiO_2 samples were coated on a glass substrate. The SEM image of Cu_2S (NP)-TiO_2 shows the uniform particle distribution of size 11 ± 2 nm. The particle size distribution obtained from these SEM images is shown in fig. S4. Atomic percentages of different metallic elements of the Cu_2S-TiO_2 sample was investigated by an energy dispersive X-ray spectrometer (EDX), as shown in fig. S5. In addition, an elemental mapping of Fig. 2(c) is presented in Fig. 2(d). These two pictures indicate the atomic percentages of Cu and Ti, S, and O inside thin film are with a stoichiometric ratio.

Transmission electron microscopy (TEM) study has been performed for detailed structural analysis which indicates the formation of Cu_2S-NP within the TiO_2 matrix, identified due to the higher contrast of Cu_2S compared to TiO_2. The distribution of particle size that is measured through this TEM study is within the range of 7–21 nm with an average size of 10 ± 3 nm. This distribution is quite close to the SEM analysis as shown in Fig. 3(b). Since, original thickness of $Li_4Ti_5O_{12}$ film is ~ 60 nm, therefore on an average 4–5 layers of Cu_2S NP can be grown within Cu_2S NP-TiO_2 thin film which is supported by Fig. 3a. High-resolution TEM (HR-TEM) image of Cu_2S (NPs)-TiO_2 (Fig.−3(c)) shows the lattice fringe formation of Cu_2S-NP and TiO_2 individually, indicates their co-existence that forms the heterojunction.

The averaged d-spacing values of Cu_2S-NP and TiO_2 have been extracted from HR-TEM images which are 0.24 and 0.35 nm, corresponding to the (102) and (101) plans of Cu_2S and TiO_2 respectively. These two planes were also observed in XRD data as well (Fig. 2a) and have been identified in selected area diffraction patterns of TEM study (Fig. 3(d)).

3.2. X-ray photoemission spectroscopy (XPS)

The X-ray photoemission spectroscopy (XPS) experiment has been carried out to identify the chemical state of the elements presented in Cu_2S-TiO_2 nanocomposite samples. The wide survey scan spectrum of XPS for the Cu_2S-TiO_2 is shown in the fig. S6 that contain Cu, O, C, Ti and S. The C peak appears due to the residual carbon from the sample. The

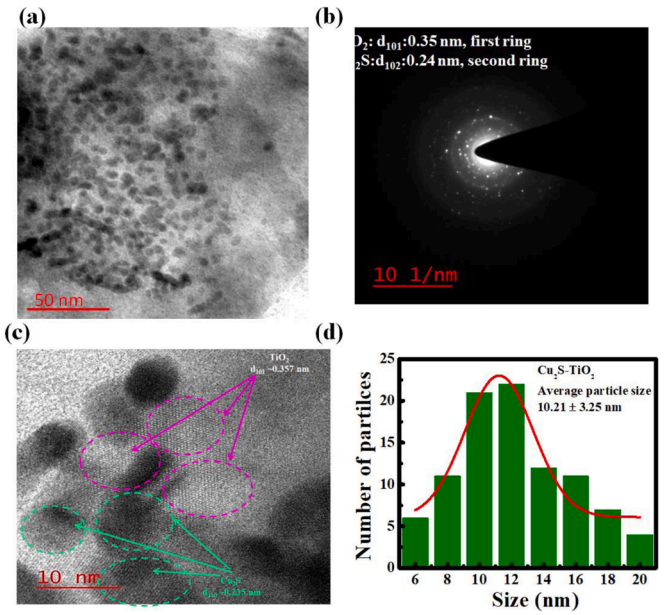

Fig. 3. (a) TEM image of Cu_2S NP-TiO_2 (b) The SAED pattern of Cu_2S NP-TiO_2 (c) HR-TEM image of Cu_2S NP-TiO_2, the white circle indicates the lattice spacing D-fringe of Cu_2S and magenta circle for TiO_2 (d) Size distribution of Cu_2S NPs inside TiO_2 thin film TEM images.

spectra of Cu2p, S2p, Ti2p, and O1s are shown in Fig. 4(a-d), respectively. Fig. 4(a) indicates that the Cu2p has two distinct peaks at 952.53 and 932.53 eV, which are originated due to the binding energy of $Cu2p_{1/2}$ and $Cu2p_{3/2}$ respectively, very similar to the reported value [14,35]. The existence of the sharp peak of $Cu2p_{3/2}$ at 932.53 eV is very close to the characteristic peak of $Cu2p_{3/2}$ for Cu(I), indicating that our sample is mainly formed due to the Cu_2S, which is also realized from XRD data. However, deconvolution of the $Cu2p_{3/2}$ peak shows that there could be a characteristic peak at 934.5 eV that may have originated from Cu(II). The existence of a weak satellite peak in between Cu $2p_{1/2}$ and $Cu2p_{3/2}$ also indicates the co-existence of CuO on the surface of the sample. [36] Since the existence of CuO is not observed in XRD data, therefore it is expected that it doesn't exist in deeper part of the sample which is also

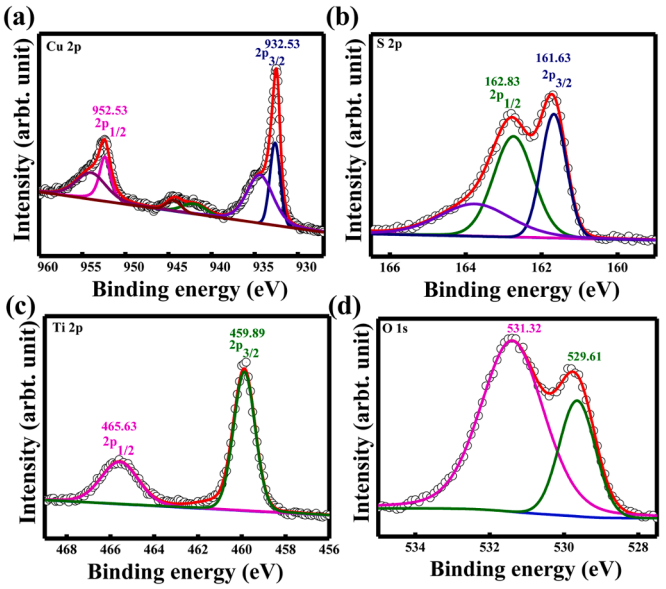

Fig. 4. X-ray photoemission spectroscopy (XPS) spectra of Cu_2S-TiO_2 sample (a) Cu 2p (b) S 2p(c) Ti 2p and (d) O 1 s.

observed in earlier publications. [36] Two peaks of Fig. 4(b) appear for S2p at 162.23 eV and 160.13 eV are very close to the characteristic peak of S^{2-}, indicating the formation of Cu_2S [35]. We have observed one extra resolvable peaks around 163.7 eV, that originates from the polysulfide species. [37,38] On the other hand, two peaks for $Ti2p_{1/2}$ and $Ti2p_{3/2}$ at 465.63 eV and 459.89 eV have been observed, which are characteristics of Ti^{+4} as presented in Fig. 4(c). Besides those peaks, two more peaks are observed for O1s at the binding energies of 531.32 eV, 529.61 eV, which are related to O in TiO_2 and oxygen vacancies respectively (Fig. 4(d)), indicating the formation of Ti-O-Ti bonding [39]. All these peak positions support earlier published data of Cu_2S--TiO_2 systems [40]. Overall, this XPS study gives additional evidence of forming Cu_2S-TiO_2 phases inside the thin film.

3.3. Photoelectrochemical H_2 generation study

The I-V characteristics of three different Cu_2S-TiO_2 photoanodes have been studied under dark and light (100 mW/m^2) conditions (Fig. 5 (a)) showing difference in current levels (light and dark conditions) by around one order for all these samples. Similar electrical behavior of M2S-TiO2 photoanodes have been reported earlier in several literatures. [41–43] This photocurrent mostly arises from the lower band gap Cu_2S NP that absorbs most of the lights in the spectrum of white light. After electron-hole generation, photogenerated electrons of Cu_2S are transferred to the conduction band of TiO_2 and FTO respectively. After reaching to FTO, electron transfer to the Pt electrode through the external circuit, whereas photogenerated holes oxidize water to oxygen molecules. The mechanism of the charge transfer process of the photoelectrochemical H_2 generation for the Cu_2S-TiO_2 system is shown in Fig. 5(b). Besides, photocurrent generation of Cu_2S-TiO_2 photoanode has been enhanced considerably by adding an underlying TiO_2 layer that boosted both H_2 evolution reaction (HER) and O_2 evolution reaction (OER) simultaneously. Out of these three photoanodes, the maximum photocurrent generation was observed with Cu_2S-TiO_2/TiO_2 NP photoanode with a current density of~36 mAcm^{-2} at −0.51 V external bias for HER and ~8.8 mA cm^{-2} at 0.4 V for OER. The maximum current density value achieved by this photoanode is much higher than previous reports on the Cu_2S-TiO_2 system under similar experimental conditions [14,44]. From this comparison, it's very clear that the charge transport rate through these in situ grown electronically coupled Cu_2S - TiO_2 nanoheterojunction is the key factor for this improvement.

Moreover, the current density of Cu_2S-TiO_2 /TiO_2 NP/FTO photoanode is more than three orders of magnitude higher than the TiO_2 (only) photoanode (0.012 mA cm^{-2}) (Fig. S7a). This improvement of the photocurrent level originated from two reasons. One important reason is the lower band gap of Cu_2S NP that enables it to absorb a wider range of spectrum of white light, which, in turn, generates a larger number of photogenerated electron-hole carriers. Similar effects have been reported for different TiO_2-metal chalcogenide based photoanode, including MoS_2/TiO_2 [45] and Ag_2S/TiO_2 [46,47], TiO_2/Z-nIn_2S_4/$Zn_{0.4}Ca_{0.6}In_2S_4$ [48]. Besides, another important factor is the higher charge (electron) transfer rate from electronically coupled Cu_2S NP to TiO_2 due to major reduction of the electron-hole recombination in the interface of Cu_2S NP/TiO_2 which is shown schematically in Fig. 5(a). Because of the lower band gap of Cu_2S NP, most of the spectrum of visible light is absorbed by it and generates a major part of photogenerated carriers (electron and hole). Subsequently photogenerated electrons of Cu_2S NPs are transferred to the CB of TiO_2 due to their energetically favorable band alignment [49,50]. Besides, the higher energy photons of visible light (mostly UV light) is absorbed by TiO_2 and contributes a fraction of the photogenerated carriers. All these photogenerated electrons are then transferred from CB of TiO_2 to the FTO electrode and finally transported to the Pt cathode where it produces H_2 gas. Simultaneously, the photogenerated hole of TiO_2 and Cu_2S NP are combined together and react with the electrolyte producing OH and H^+ Eq. (2)–(9). Afterword, H^+ of electrolytes accept electron from the Pt

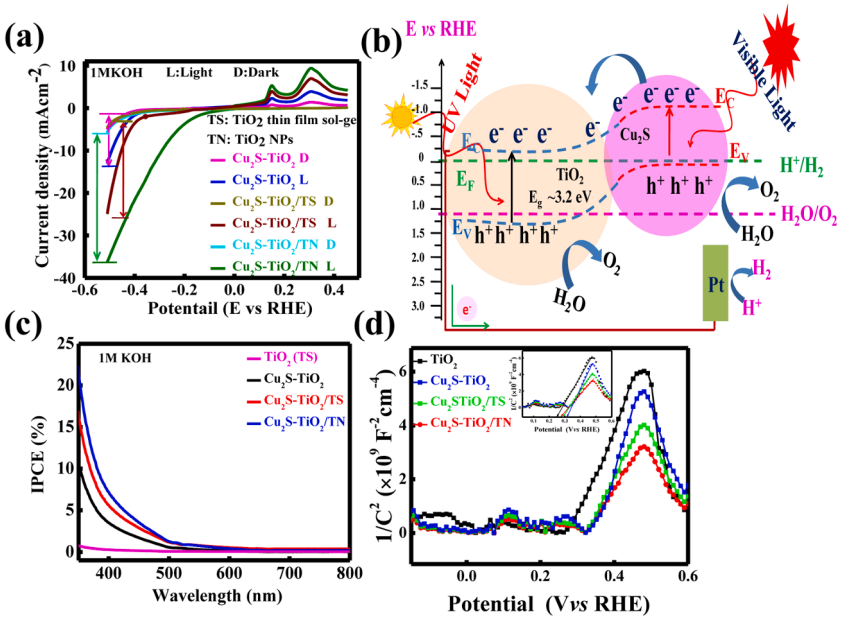

Fig. 5. (a): Current density vs. (V vs. RHE) potential of different Cu_2S-TiO_2 thin film under light and dark in 1 M KOH. (b)The schematic diagram of the photocatalytic water splitting mechanism by Cu_2S-TiO_2 based photoanode. (c) IPCE of bare TiO_2, Cu_2S-TiO_2 with three different substrates. (d) The Mott−Schottky (M-S) plot for various photoanodes under 1 kHz operation in dark condition.

electrode to form a H atom and subsequent H_2 molecule. Based on the observation of our photo-electrochemical experiment, these charge transport processes were enhanced further by an additional TiO_2 under layer due to the larger area of heterojunction formation between Cu_2S and TiO_2.

In electrolyte

$$H_2O \rightarrow OH^- + H^+ \quad (2)$$

At anode

$$TiO_2 + hv\ (UV\ light) \rightarrow CB_{Tio2}\ (e^-) + VB_{Tio2}\ (h^+) \quad (3)$$

$$Cu_2S + hv\ (visible\ light) \rightarrow CB_{Cu_2S}\ (e^-) + VB_{Cu_2S}\ (h^+) \quad (4)$$

$$CB_{cu2s}\ (e^-) + TiO_2 \rightarrow VB_{cu2s}\ (h^+) + CB_{Tio2}\ (e) \quad (5)$$

$$CB_{cu2s}\ (e^-) + CB_{Ti02}\ (e^-) \rightarrow VB_{cu2s}\ (h^+, h^+) + CB_{Tio2}\ (e^-, e^-) \quad (6)$$

$$VB_{cu2s}\ (h^+) + OH^- \rightarrow OH + H^+ \quad (7)$$

$$4OH \rightarrow 2H_2O + O_2 \quad (8)$$

At counter electrode

$$2H^+ + 2e^- \rightarrow H_2 \quad (9)$$

The photocurrent generation rate in different wavelengths of light was investigated by measuring 'incident photon to converted electron' (IPCE) data for various photoanodes. A comparative performance of IPCE data of three photoanodes under −1.0 V bias has been shown in Fig. 5(c). This study indicates that the IPCE data of all Cu_2S-TiO_2 photoanode are quite similar, with high photocurrent generation in the spectral range of 350–500 nm. In contrast to this data, TiO_2 (sol-gel) photoanode generates photocurrent mostly below 400 nm, which is expected due to its larger bandgap (~3.3 eV). Therefore, this comparative IPCE study indicates that the major part of the photocurrent originates from the Cu_2S NP, which is associated with H_2 generation. Moreover, the maximum value of IPCE has been achieved for the Cu_2S-TiO_2 /TiO_2 NPs/FTO photoanode (~ 22.56% at 350 nm). This experiment also indicated that the underlying TiO_2 layer is beneficial for photogenerated charge transfer to the FTO electrode. Compared to sol-gel derived TiO_2 thin film, TiO_2–NP film shows higher values of IPCE which is due to the more compact and crystalline nature of TiO_2 thin film that has lower internal trap states.

The Mott−Schottky (M-S) study was performed for better understanding of charge transport (electron) phenomena of photoanodes (Fig. 5(d)). This experiment was carried out under dark conditions at 1 kHz frequency. This study gives the experimental value of flat band potential (E_{FD}) that originated at the interface of the semiconductor and electrolyte and the surface charge density (N_D) values following the Mott−Schottky equation [32];

$$\frac{1}{C^2} = \frac{2}{e\ \varepsilon_0\ \varepsilon_r\ N_D}\left(E_{app} - E_{FD} - \frac{kT}{e}\right) \quad (10)$$

Where, C, k, e, T are interfacial capacitance, Boltzmann constant (1.3807×10^{-23}); electronic charge (1.6×10^{-19}coulomb), and temperature of the system (~300 K) respectively. The M-S data of various photoanodes follows a linear variation of $1/C^2$ with external potential with a positive slope that implies the n-type behavior of the semiconductor. The E_{FD} of different photoanodes were measured from the intersection of the slope with the X-axis which shows a positive shift for all Cu_2S-TiO_2 photoanodes than the TiO_2 photoanode, which indicates a large variation of charge transfer rate because of the formation of Cu_2S NP. Out of four different photoanodes, the maximum value of E_{FD} has been achieved for Cu_2S-TiO_2/TiO_2 NPs photoanode, indicating its better charge transfer performance with respect to the other photoanodes. Besides, the surface charge densities (N_D) of these four photoanodes have been extracted from the M-S plot by using the following equation. [32]

$$N_D = \frac{2}{e\varepsilon_0\ \varepsilon_r} \frac{dE}{d\left(\frac{1}{C^2}\right)} \quad (11)$$

This calculation shows a large enhancement of N_D for Cu_2S-TiO_2 thin film with respect to TiO_2 (only) thin film and the highest value has been determined for Cu_2S-TiO_2/TiO_2/FTO NPs photoanode. This higher value of N_D is responsible for the reduction in the ohmic resistance as well as its higher rate of charge transfers from photoanode to the FTO electrode. The summary of E_{FD} and N_D values for different photoanodes are shown in table S1.

Photoresponse of different photoanodes under dark and 100 mW/

Table 1
Summary of R_S, R_1 and R_2 for all three Cu_2S-TiO_2 photoanode under dark and light conditions.

Device structure	Rs (kΩ)		R_1 (kΩ)		R_2 (kΩ)	
	dark	light	dark	light	dark	light
Cu_2S-TiO_2	0.050	0.010	1.490	1.050	4.216	1.467
Cu_2S-TiO_2/TS	0.024	0.008	1.201	0.886	3.367	0.884
Cu_2S-TiO_2/TN	0.025	0.007	1.080	0.678	2.133	0.694

cm^2 white light with −0.5 V applied bias is shown in Fig. 6(a). This data indicates that the photoresponse of all photoanodes are repeatable. Besides, the Cu_2S-TiO_2/TiO_2(NPs)/FTO photoanode has a quite fast rise and decay time of 2.10 s. and 2.61 s. respectively. These values are fairly faster than other photoanodes due to its higher rate of charge transfer. Summary of photoresponce performance are given in table S2. The stability test of Cu_2S-TiO_2/TiO_2(NPs)/FTO photoanode was studied for 200 min under continuous white light illumination. This data indicates almost constant photocurrent generation over that time scale, indicating its reasonably good stability (Fig. 6(b)).

The electrochemical impedance spectroscopy (EIS) performance of different Cu_2S-TiO_2 based photoanodes under dark and white light illumination are demonstrated in Fig. 6(c). A large variation of EIS data under two different optical conditions are observed in all cases, implying a very significant variation of internal resistances because of light illumination. The EIS data also shows two semicircles formation for all Cu_2S-TiO_2 based photoanodes. Comparative EIS data also indicates that the semicircle diameter with Cu_2S-TiO_2/TiO_2 NP/FTO photoanode has the least value compared to two other Cu_2S-TiO_2 based photoanodes under both dark and light conditions. This result implies that the internal resistance of Cu_2S-TiO_2/TiO_2 NP/FTO photoanode has much lower value than other two photoanodes. Moreover, the smallest semicircles of EIS data of this photoanode also implies higher charge transfer and electron hole separation rate with respect to others. [51] All EIS data are fitted to according to its equivalent circuit, which is given in the inset of Fig. 6(c). This equivalent circuit consists of the electrolyte resistance (R_S) in series with the parallel connection of interfacial charge-transfer resistance of the photoanode/electrolyte interface (R_1, R_2) and double-layer capacitance (C_1, C_2) related to the charge transfer process. The values of R_S, R_1 and R_2 for all Cu_2S-TiO_2 photoanode under dark and light are shown in table-1. Comparative EIS studies between pure TiO_2 and three other Cu_2S-TiO_2 based photoanodes are shown in the supporting document (fig. S7b), which indicates that the growth of Cu_2S NPs inside TiO_2 film reduces the internal resistance of the photoanode dramatically.

The hydrogen and oxygen generation rate has been studied under steady state irradiation of white light with intensity of 100 mW/cm^2 as shown in Fig. 7(a). This study has been performed with two different Cu_2S-TiO_2 based photoanodes. One of them is with TiO_2 (NPs) layer, and the other one is without TiO_2 (NPs) layer. Besides, performance of a TiO_2 (sol gel)-based photoanode has been shown for comparison. Fig. 7 (b) shows the volumetric hydrogen and oxygen production under 100 mW/cm^2, white light illumination for five successive cycles by Cu_2S-TiO_2/TiO_2 NPs photoanode. As observed, the cyclic H_2 generation rate is quite similar in all different cycles with an average value of 55 ± 5 μml/cm^2/hour. Similar behavior has been observed for O_2 generation with an average rate of 27 ± 5 μml/cm^2/hour.

In summary, wide area Cu_2S (NP)–TiO_2 nano heterojunction thin film has been deposited by a solution-processed method. This nano heterojunction growth was successfully achieved through three successive steps including deposition of $Li_4Ti_5O_{12}$ ceramic thin film and subsequent replacement of Li^+ by Cu^+ through an ion-exchange process to form $Cu_4Ti_5O_{12}$ thin film. Afterwards, $Cu_4Ti_5O_{12}$ thin-film undergoes a chemical conversion of Cu^+ to Cu_2S in presence of $NaBH_4$ to form Cu_2S-TiO_2 nano heterojunction. This typical growth process allows us to form a larger interface area of Cu_2S/TiO_2 nano heterojuction with a least number of interfacial trap states. The heterojunction formation of Cu_2S-TiO_2 was identified by electron microscopes like TEM and SEM. Coexistence of Cu_2S-TiO_2 was identified by XRD, UV/Vis absorption and XPS study. Photoelectrochemical performance of Cu_2S-TiO_2 nano heterojuction film was studied to realize its suitability for H_2 production. For this purpose, Cu_2S-TiO_2 thin film coated photoanodes were fabricated over three substrates such as FTO, TiO_2 (sol gel)/FTO and TiO_2

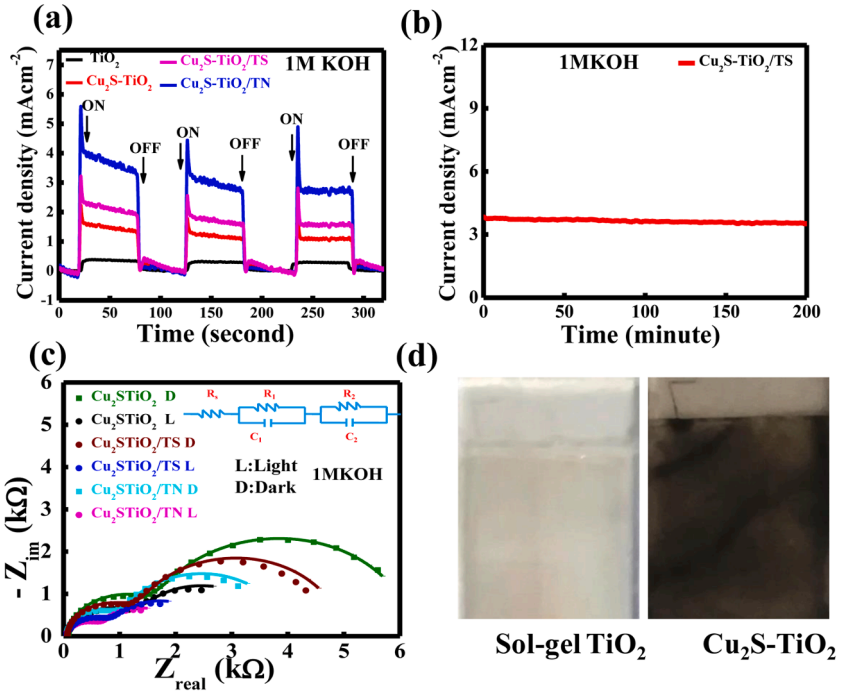

Fig. 6. (a) Photo response data under 100 mW/cm^2 white light and dark with −0.5 V external bias in 1 M KOH medium, (b) Photo stability performance of Cu_2S-TiO_2/TiO_2/FTO photoanode under continues white light (1 sun) illumination (c) electrochemical impedance spectroscopy (EIS) data for different Cu_2S-TiO_2 photoanodes under light and dark condition (d) images of Cu_2S-TiO_2 and TiO_2 (NPs) photoanodes.

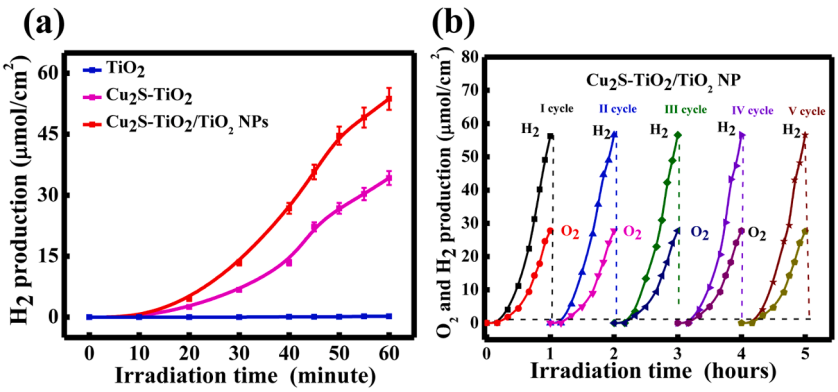

Fig. 7. **(a)** Volumetric hydrogen generation data under white light (100 mW/cm^2) for three different photoanodes. (b) volumetric hydrogen and oxygen generation under white light (100 mW/cm^2) for five successive cycle by Cu_2S-TiO_2/TiO_2 NPs photoanode.

NP/FTO. A comparative photoelectrocatalytic study showed that the photoanode on TiO_2 NP/FTO substrate generates photocurrent of density of 36 mA cm^{-2} under 0.5 V applied bias, which is much higher than two other Cu_2S-TiO_2 based photoanodes and ~3600 times greater than TiO_2 (only) photoanode. Volumetric measurement shows that this H_2 and O_2 generation rate is ~ 55 ± 5 and 27 ± 5 μmol/cm^2/hour respectively. This photocurrent density and H_2 generation rate is considerably higher than previously reported Cu_2S-TiO_2 systems. Besides, this Cu_2S-TiO_2 nano heterojunction based photoanode shows a very good stability of photocurrent generation over the period of 1.5 h. This nano heterojunction growth process can be extended in future for other chalcogenides/metal oxide heterojunction combinations for different energy harvesting devices.

Declaration of Competing Interest

The authors declare that they have no known competing financial interests or personal relationships that could have appeared to influence the work reported in this paper.

Acknowledgments

B. N. Pal thanked "SERB(DST)," India (EMR/2015/000689) and Center for Energy & Resources Development (CERD), IIT (BHU) for their partial financial support. Authors are also grateful to Central Instrument Facility centre, IIT (BHU), for providing instrument support for different materials characterization such as TEM, SEM and XRD. S Biring acknowledges financial support from the Ministry of Science and Technology, Taiwan (MOST 110-2221-E-131-019).

Supplementary materials

Supplementary material associated with this article can be found, in the online version, at doi:10.1016/j.surfin.2021.101660.

References

[1] X. Chen, S. Shen, L. Guo, S.S. Mao, Semiconductor-based photocatalytic hydrogen generation, Chem. Rev. 110 (11) (2010) 6503–6570.
[2] X. Chen, S.S. Mao, Titanium dioxide nanomaterials: synthesis, properties, modifications, and applications, Chem. Rev. 107 (7) (2007) 2891–2959.
[3] M. Dahl, Y. Liu, Y. Yin, Composite titanium dioxide nanomaterials, Chem. Rev. 114 (19) (2014) 9853–9889.
[4] S. Wannapop, A. Somdee, Enhanced visible light absorption of TiO2 nanorod photoanode by NiTiO3 decoration for high-performance photoelectrochemical cells, Ceram. Int. 46 (16) (2020) 25758–25765. Part A.
[5] J. Schneider, M. Matsuoka, M. Takeuchi, J. Zhang, Y. Horiuchi, M. Anpo, D. W. Bahnemann, Understanding TiO2 photocatalysis: mechanisms and materials, Chem. Rev. 114 (19) (2014) 9919–9986.
[6] S.J.A. Moniz, S.A. Shevlin, D.J. Martin, Z.-X. Guo, J. Tang, Visible-light driven heterojunction photocatalysts for water splitting – a critical review, Energy Environ. Sci. 8 (3) (2015) 731–759.
[7] C.M. Magdalane, G.M.A. Priyadharsini, K. Kaviyarasu, A.I. Jothi, G.G. Simiyon, Synthesis and characterization of TiO2 doped cobalt ferrite nanoparticles via microwave method: investigation of photocatalytic performance of congo red degradation dye, Surf. Interfaces 25 (2021), 101296.
[8] S.V. Singh, M.P. Kumar, S. Anantharaj, B. Mukherjee, S. Kundu, B.N. Pal, Direct evidence of an efficient plasmon-induced hot-electron transfer at an in situ grown Ag/TiO2 interface for highly enhanced solar H2 generation, ACS Appl. Energy Mater. 3 (2) (2020) 1821–1830.
[9] R. Reichert, Z. Jusys, R.J. Behm, Au/TiO2 Photo(electro)catalysis: the role of the au cocatalyst in photoelectrochemical water splitting and photocatalytic H2 evolution, J. Phys. Chem. C 119 (44) (2015) 24750–24759.
[10] Y. Zhou, H. Ding, J. Liu, A.M. LaChance, M. Xiao, Y. Meng, L. Sun, Gold nanoparticles immobilized on single-layer α-zirconium phosphate nanosheets as a highly effective heterogeneous catalyst, Adv. Compos. Hybrid Mater. 2 (3) (2019) 520–529.
[11] L. Guo, C. Zhong, J. Cao, Y. Hao, M. Lei, K. Bi, Q. Sun, Z.L. Wang, Enhanced photocatalytic H2 evolution by plasmonic and piezotronic effects based on periodic Al/BaTiO3 heterostructures, Nano Energy 62 (2019) 513–520.
[12] E.C. Neyts, K. Ostrikov, M.K. Sunkara, A. Bogaerts, Plasma catalysis: synergistic effects at the nanoscale, Chem. Rev. 115 (24) (2015) 13408–13446.
[13] K. Chen, X. Feng, R. Hu, Y. Li, K. Xie, Y. Li, H. Gu, Effect of Ag nanoparticle size on the photoelectrochemical properties of Ag decorated TiO2 nanotube arrays, J. Alloys Compd. 554 (2013) 72–79.
[14] G. Liu, T. Schulmeyer, A. Thissen, A. Klein, W. Jaegermann, In situ preparation and interface characterization of TiO2/Cu2S heterointerface, Appl. Phys. Lett. 82 (14) (2003) 2269–2271.
[15] K. Nagasuna, T. Akita, M. Fujishima, H. Tada, Photodeposition of Ag2S quantum dots and application to photoelectrochemical cells for hydrogen production under simulated sunlight, Langmuir 27 (11) (2011) 7294–7300.
[16] X. Zheng, S. Das, Y. Gu, S. Liu, J. Zhao, Optimal engineering of CdS/PbS co-sensitized TiO2 nanotube arrays for enhanced photoelectrochemical performance, Ceram. Int. 46 (8) (2020) 12050–12058. Part B.
[17] M. Mao, J. Xu, Y. Li, Z. Liu, Hydrogen evolution from photocatalytic water splitting by LaMnO3 modified with amorphous CoSx, J. Mater. Sci. 55 (8) (2020) 3521–3537.
[18] J.-H. Park, P. Ramasamy, S. Kim, Y.K. Kim, V. Ahilan, S. Shanmugam, J.-S. Lee, Hybrid metal–Cu2S nanostructures as efficient co-catalysts for photocatalytic hydrogen generation, Chem. Commun. 53 (22) (2017) 3277–3280.
[19] M.-R. Gao, J. Jiang, S.-H. Yu, Solution-based synthesis and design of late transition metal chalcogenide materials for oxygen reduction reaction (ORR), Small 8 (1) (2012) 13–27.
[20] S. Qian, C. Wang, W. Liu, Y. Zhu, W. Yao, X. Lu, An enhanced CdS/TiO2 photocatalyst with high stability and activity: effect of mesoporous substrate and bifunctional linking molecule, J. Mater. Chem. 21 (13) (2011) 4945–4952.
[21] M.Z. Ansari, S. Singh, N. Khare, Visible light active CZTS sensitized CdS/TiO2 tandem photoanode for highly efficient photoelectrochemical hydrogen generation, Sol. Energy 181 (2019) 37–42.
[22] M. Zhong, J. Shi, F. Xiong, W. Zhang, C. Li, Enhancement of photoelectrochemical activity of nanocrystalline CdS photoanode by surface modification with TiO2 for hydrogen production and electricity generation, Sol. Energy 86 (2) (2012) 756–763.
[23] Y. Chen, D. Yang, Y. Gao, R. Li, K. An, W. Wang, Z. Zhao, X. Xin, H. Ren, Z. Jiang, On-Surface bottom-up construction of COF nanoshells towards photocatalytic H_2 production, in: Research 2021, 2021, 9798564.
[24] H. He, J. Lin, W. Fu, X. Wang, H. Wang, Q. Zeng, Q. Gu, Y. Li, C. Yan, B.K. Tay, MoS2/TiO2 edge-on heterostructure for efficient photocatalytic hydrogen evolution, Adv. Energy Mater. 6 (14) (2016), 1600464.
[25] Y.-X. Yu, L. Pan, M.-K. Son, M.T. Mayer, W.-D. Zhang, A. Hagfeldt, J. Luo, M. Grätzel, Solution-processed Cu2S photocathodes for photoelectrochemical water splitting, ACS Energy Lett. 3 (4) (2018) 760–766.

[26] F. Säuberlich, A. Klein, Band alignment at oxide semiconductor interfaces, MRS Online Proc. Library Arch. 763 (2003).
[27] S.C. Riha, R.D. Schaller, D.J. Gosztola, G.P. Wiederrecht, A.B.F. Martinson, Photoexcited carrier dynamics of Cu2S thin films, J. Phys. Chem. Lett. 5 (22) (2014) 4055–4061.
[28] L. Tang, Y. Deng, G. Zeng, W. Hu, J. Wang, Y. Zhou, J. Wang, J. Tang, W. Fang, CdS/Cu2S co-sensitized TiO2 branched nanorod arrays of enhanced photoelectrochemical properties by forming nanoscale heterostructure, J. Alloys Compd. 662 (2016) 516–527.
[29] Y.-J. Hao, Q.-Y. Lai, J.-Z. Lu, H.-L. Wang, Y.-D. Chen, X.-Y. Ji, Synthesis and characterization of spinel Li4Ti5O12 anode material by oxalic acid-assisted sol–gel method, J. Power Sources 158 (2) (2006) 1358–1364.
[30] D. Wang, Y. Li, Controllable synthesis of Cu-based nanocrystals in ODA solvent, Chem. Commun. 47 (12) (2011) 3604–3606.
[31] K. Iwashina, A. Iwase, Y.H. Ng, R. Amal, A. Kudo, Z-schematic water splitting into H2 and O2 using metal sulfide as a hydrogen-evolving photocatalyst and reduced graphene oxide as a solid-state electron mediator, J. Am. Chem. Soc. 137 (2) (2015) 604–607.
[32] N. Kodan, K. Agarwal, B.R. Mehta, All-oxide α-Fe2O3/H:tiO2 heterojunction photoanode: a platform for stable and enhanced photoelectrochemical performance through favorable band edge alignment, J. Phys. Chem. C 123 (6) (2019) 3326–3335.
[33] D. Reyes-Coronado, G.R. Gattorno, M.E. Pesqueira, R. de Coss, G. Oskam, Phase-Pure TiO2 Nanoparticles: Anatase, Brookite and Rutile, Nanotechnology 19 (2008), 145605.
[34] L. Zhu, Z.-D. Meng, W.-C. Oh, MWCNT-based Ag 2 S-TiO 2 nanocomposites photocatalyst: ultrasound-assisted synthesis, characterization, and enhanced catalytic efficiency, J. Nanomater. (2012) 5, 2012.
[35] H. Huang, F. Li, H. Wang, X. Zheng, The size controlled synthesis of Cu2S/P25 hetero junction solar-energy-materials and their applications in photocatalytic degradation of dyes, RSC Adv. 7 (79) (2017) 50056–50063.
[36] M. Li, R. Zhao, Y. Su, Z. Yang, Y. Zhang, Carbon quantum dots decorated Cu2S nanowire arrays for enhanced photoelectrochemical performance, Nanoscale 8 (16) (2016) 8559–8567.
[37] I. Shown, S. Samireddi, Y.-C. Chang, R. Putikam, P.-H. Chang, A. Sabbah, F.-Y. Fu, W.-F. Chen, C.-I. Wu, T.-Y. Yu, P.-W. Chung, M.C. Lin, L.-C. Chen, K.-H. Chen, Carbon-doped SnS2 nanostructure as a high-efficiency solar fuel catalyst under visible light, Nat. Commun. 9 (1) (2018) 169.
[38] M. Fantauzzi, B. Elsener, D. Atzei, A. Rigoldi, A. Rossi, Exploiting XPS for the identification of sulfides and polysulfides, RSC Adv. 5 (93) (2015) 75953–75963.
[39] V.N. Rao, N.L. Reddy, M.M. Kumari, P. Ravi, M. Sathish, K. Kuruvilla, V. Preethi, K. R. Reddy, N.P. Shetti, T.M. Aminabhavi, Photocatalytic recovery of H2 from H2S containing wastewater: surface and interface control of photo-excitons in Cu2S@TiO2 core-shell nanostructures, Appl. Catal. B 254 (2019) 174–185.
[40] S. Ding, X. Yin, X. Lü, Y. Wang, F. Huang, D. Wan, One-step high-temperature solvothermal synthesis of TiO2/sulfide nanocomposite spheres and their solar visible-light applications, ACS Appl. Mater. Interfaces 4 (1) (2012) 306–311.
[41] Y. Cho, M. Park, J.K. Kim, S. Kim, H. Suk Jung, J.H. Park, Electrochemically controlled CdS@CdSe nanoparticles on ITO@TiO2 dual core–shell nanowires for enhanced photoelectrochemical hydrogen production, Appl. Surf. Sci. 505 (2020), 144569.
[42] M. Zhang, F. Li, D. Benetti, R. Nechache, Q. Wei, X. Qi, F. Rosei, Ferroelectric polarization-enhanced charge separation in quantum dots sensitized semiconductor hybrid for photoelectrochemical hydrogen production, Nano Energy 81 (2021), 105626.
[43] B. Chang, G. Zhao, Y. Shao, L. Zhang, B. Huang, Y. Wu, X. Hao, Photo-enhanced electrocatalysis of sea-urchin shaped Ni3(VO4)2 for the hydrogen evolution reaction, J. Mater. Chem. A 5 (34) (2017) 18038–18043.
[44] L. An, P. Zhou, J. Yin, H. Liu, F. Chen, H. Liu, Y. Du, P. Xi, Phase transformation fabrication of a Cu2S nanoplate as an efficient catalyst for water oxidation with glycine, Inorg. Chem. 54 (7) (2015) 3281–3289.
[45] M. Mehta, A.P. Singh, S. Kumar, S. Krishnamurthy, B. Wickman, S. Basu, Synthesis of MoS2-TiO2 nanocomposite for enhanced photocatalytic and photoelectrochemical performance under visible light irradiation, Vacuum 155 (2018) 675–681.
[46] X.-b. Ning, S.-s. Ge, X.-t. Wang, H. Li, X.-r. Li, X.-q. Liu, Y.-l. Huang, Preparation and photocathodic protection property of Ag2S-TiO2 composites, J. Alloys Compd. 719 (2017) 15–21.
[47] S. Ghafoor, S. Ata, N. Mahmood, S.N. Arshad, Photosensitization of TiO2 nanofibers by Ag2S with the synergistic effect of excess surface Ti3+ states for enhanced photocatalytic activity under simulated sunlight, Sci. Rep. 7 (2017).
[48] X. Shi, C. Dai, X. Wang, P. Yang, L. Zheng, Z. Zhao, H. Zheng, Facile construction TiO2/ZnIn2S4/Zn0.4Ca0.6In2S4 ternary hetero-structure photo-anode with enhanced photo-electrochemical water-splitting performance, Surf. Interfaces 26 (2021), 101323.
[49] Y. Zhang, Q. Zhou, J. Zhu, Q. Yan, S.X. Dou, W. Sun, Nanostructured Metal Chalcogenides for Energy Storage and Electrocatalysis, Adv. Funct. Mater. 27 (35) (2017), 1702317.
[50] R. Guan, H. Zhai, J. Li, Y. Qi, M. Li, M. Song, Z. Zhao, J. Zhang, D. Wang, H. Tan, Reduced mesoporous TiO2 with Cu2S heterojunction and enhanced hydrogen production without noble metal cocatalyst, Appl. Surf. Sci. 507 (2020), 144772.
[51] Y. Bessekhouad, R. Brahimi, F. Hamdini, M. Trari, Cu2S/TiO2 heterojunction applied to visible light Orange II degradation, J. Photochem. Photobiol. A 248 (2012) 15–23.